# Supporting Information

Fridman et al. 10.1073/pnas.1320969111

## SI Text

**Connectivity of Segregated Basal Ganglia–Thalamostriatal and Thalamocortical Mesocircuit (Fig. S1).** On the left of the figure, the illustration shows the pattern of distribution of reciprocal central thalamic-cortical connections to the frontal and parietal cortices and the diverse cortical inputs to the different substructures of the striatal complex [i.e., ventral striatum (VST), associative striatum (AST), and sensorimotor striatum (SMST)]. On the right of the figure, the thalamostriatal-striatopallidal-pallidothalamic microcircuit loops are illustrated. Red arrows represent excitatory projections and white arrows inhibitory projections. Following multifocal brain injuries that produce widespread deafferentation or neuronal cell loss, the thalamocortical projections of the central thalamus, along with the striatum and globus pallidus, are proposed to play an important role in observed reduction of cerebral metabolism in this mesocircuit following different mechanisms of brain injury (1).

**Defining the Functional Subdivisions of the Striatum.** For all normal subjects and patient analyses, striatal and thalamic regions of interest (ROIs) were hand drawn onto 3D MRI. A high-resolution T1 image was reoriented to the Anterior Commissure-Posterior Commissure (AC-PC) line. On a *y* axis view, we set a plane to separate pre- and postcommissural structures and traced a line between the outer edge of the putamen and the center of the portion of the AC passing through the lower level of the internal capsule (cf. figure 1 in ref. 2). Deep gray structures located anterior and below this previously defined intersection were defined as the VST; precommissural putamen and the caudate above the intersection constituted the AST; and postcommissural putamen composed the SMST. The globus pallidus (GP) was identified by its characteristic tissue boundaries in normal volunteers (NVs) and most of the patient subjects. In patients for whom GP boundaries were unclear, the limits of GP were inferred by the internal wall of the AST and SMST and the external wall of the noncentral thalamus (non-c-TH). Further separation of the GP into its ex and internal components was not possible for the patient subjects and therefore GP was not further subparcellated in the NV group.

It is important to note that the subdivision of the striatum is based on its cortical loops: VST by its known connectivity with the ventromedial prefrontal cortex (vmPFC), orbitofrontal cortex (OFC), and anterior cingulate cortex (aCGc) (3); AST by its known connectivity with the dorsolateral prefrontal cortex (dlPFC), rostral premotor cortex (PMC), inferior posterior parietal cortex (iPPc) and superior posterior parietal cortex (sPPc), and superior temporal gyrus (4); and SMST by its known connectivity with primary sensorimotor cortex (SM1) and caudal PMC (5).

**Defining the Central Thalamus Using $D_2$-Like Receptor Expression in NVs with [$^{11}$C]raclopride-PET.** Currently, no automatic method exists to separate between different substructures of the thalamus (TH). Moreover, automatic segmentation for gray matter (GM), white matter (WM), and cerebrospinal fluid (CSF) within high-resolution T1 MRI images using standard methods (6) to delimit the thalamus underestimates the real extension of the structure in NVs (Fig. S3 *A* and *B*). One possible reason underlying this limitation may be the external to internal decaying gradient of paramagnetic intensity observed across the healthy TH in standard T1-MRI sequences.

It worth noting that using standard T1-MRI sequences, the substantia nigra (SN), an additional deep brain gray structure, shows a similarly low paramagnetic signal as seen in the internal aspect of the TH (Fig. S3 *C–E*). It is known that in the SN this intensity is due to neuromelanin, a black pigment produced during dopamine (DA) synthesis (7). Although thus far this association has not been explored for the TH, many studies demonstrate a moderately high density of thalamic DA receptors (8–12). Interestingly, the $D_2$-like receptors ($D_2$ and $D_3$ receptors), the most prominent subclass in the human TH, are concentrated in the central thalamus, specifically the intralaminar and paralaminar nuclei of the TH (13).

We propose that the reduced size of the TH produced by automatic GM segmentation may thus represent an actual separation of the regional distribution of DA, and therefore, demarcate the separation of the c-TH and the non-c-TH. Specifically, based on the published literature (8–12), we expected to identify greater expression of $D_2$-like receptors in the c-TH compared with thalamic tissue of the non-c-TH.

We analyzed the expression of $D_2$-like receptors in eight NVs (26.0 ± 5.5 y; eight females) from a previously reported [$^{11}$C]raclopride-PET study (for data acquisition and methods, see ref. 14). After manual realignment of the anatomical MRI to the AC-PC line, the entire right and left TH were manually drawn (Fig. 1). We then applied a probability map for GM, WM, and CSF (sampling distance, 5 mm; bias regularization, light; cleanup threshold, light) using P-MODE v.3.309 (PMOD Technologies) and used the resulting GM mask as applied to the previously defined TH ROI to delimit central structures (c-TH); the remaining portion of the original drawn TH ROI exceeding the c-TH was considered the non-c-TH (Fig. S3*C*).

[$^{11}$C]raclopride-PET data were realigned and coregistered to the 3D individual anatomical MRI using a rigid matching method (dissimilarity function: normalized mutual information with a trilinear interpolation method). A dynamic analysis of PET signal was done using the simplified reference tissue model with the cerebellum as a reference tissue (15). Binding potential ($BP_{nd}$) was obtained for the entire TH ROI, c-TH, and non-c-TH and fitted for R1 and k2′. Results were expressed as a delta change function of $BP_{nd}$ within c-TH and non-c-TH

$$\Delta BP_{nd} \text{ c-TH or non-c-TH} = 100 \times (BP_{nd} \text{ of the entire TH} - BP_{nd} \text{ of the c-TH or non-c-TH}) / BP_{nd} \text{ of the entire TH.}$$

Statistical analysis was done using a factorial ANOVA with region (c-TH and non-c-TH) and side (right and left) as factors and $\Delta BP_{nd}$ as the dependent variable. Significance was set at $P < 0.05$.

**Results.** There was a significant effect for region ($F = 32.4$; $P < 0.0001$), but not for side [$F = 0.9$; $P$ = not significant (NS)] or their interaction ($F = 0.3$; $P$ = NS). Specifically, $\Delta BP_{nd}$ for the right c-TH showed an increment of the $BP_{nd}$ compared with that obtained from the non-c-TH (8.0 ± 3.4 and −4.5 ± 2.2, respectively; $P = 0.0079$). A similar effect was observed for the left c-TH compared with the left non-c-TH (10.9 ± 2.8 and −7.1 ± 2.0, respectively; $P = 0.0002$; Fig. S3*F*).

***Brief discussion.*** The results of this analysis show a clear distinction of expression of $D_2$-like receptors within structures of the c-TH compared with those of the non-c-TH as defined by our procedures. Our results support this functional segmentation method for intrathalamic structures in NVs based on the $D_2$-like receptor distributions.

***Defining the c-TH glucose metabolism rate in severely brain-injured patients when segmentation fails to separate c-TH from non-c-TH.*** Using the above probabilistic map segmentation approach for GM, WM, and CSF measured from high-resolution anatomical MRIs in our pool of severely brain-injured (BI) patients, we were able to achieve the automatic separation of the c-TH and non-c-TH in all

but three image sets. For these remaining cases, we applied a mask created from an averaging of the eight normal subject $D_2$-like receptor ROI templates of c-TH and non-c-TH segmentations. We then applied this mask to the thalami in these three subjects to identify the c-TH and non-c-TH. Specifically, all 3D anatomical MRI from the above described [$^{11}$C]raclopride-PET were normalized to the MNI space and averaged across to create our own template (Rac8) for the TH, c-TH, and non-c-TH. Then, the three BI cases were individually normalized to the Rac8 template to obtain a spatial transformation matrix. Last, using this matrix, we applied an inverse transformation (− matrix) of Rac8-c-TH and Rac8-non-c-TH ROIs to transpose them into the individual BI natural space.

**Partial Volume Effect Analysis (Fig. S2).** The relatively small size of the SMST and particularly the GP and the proximity of these structures raised concerns about possible contamination of the GP region of interest from activity originating in the SMST. To address this potential confound, we carried out the following analyses. First, because regions are preidentified as 3D volumes from the MRI, each region can be analyzed as an independent geometric structure. We first assumed a uniform activity distribution within each region and formed the geometric transfer matrix (GTM) (16), which places the FDG-PET data onto the MRI and calculated the true activity in each region in isolation. We then estimated the recovery of these true values and potential contamination associated with uncorrected images.

The first step of this analysis was to form the GTM according to ref. 16 to restrict the partial volume correction to the signal of the true objects, which are constituted by the hand-drawn volumes of interest (VOIs) for each structure. The relationship of measured PET values (affected by the partial-volume effect) to the true PET values is given by the matrix equation below with the following notations:

$$C_{\text{measured}}(j) = GTM(i,j)^{-1}\ C_{\text{true}}(i)$$

$C_{true}$, vector of the true average activity concentration in the different VOIs of interest (the vector length n equals the number of object VOIs); $C_{measured}$, actually measured average activity concentration in the different VOIs; and GTM, GTM that describes the spillover among all of the VOIs. The matrix is square with nxn weighting elements *wi,j*, which express the fraction of true activity spilled over from VOIi into VOIj. In practice, *wi,j* is calculated as follows: a binary map is created with 1 in all pixels of VOIi and 0 elsewhere. The map is convolved with the imaging point-spread function (PSF), and in the resulting spillover map, the average of all VOIj pixels calculated.

The GTM equation above represents a system of linear equations. Once the weights have been calculated, the system can be solved for the true values $C_{true}$ by matrix inversion. Rousset et al. (16) have shown that this algorithm is robust to noise propagation during the correction process.

**Functional Cortical ROIs Definition (Fig. S4).** We applied the automated anatomical labeling [AAL (17)] cortical ROIs. Cortical regions were then further grouped into larger functional subsets to reduce the number of comparisons and emphasize functionally similar regions in evaluating variations across the BI subject pool's structural injury patterns. Specifically, frontal cortices were regrouped into five sets of major regions: orbitofrontal cortex (OFC), ventromedial prefrontal cortex (vmPFC), and dorsolateral prefrontal cortex (dlPFC) based on their contributions to reward and decision making (18), social cognition (19), and attention, working memory, and action suppression (20–22), respectively; a single premotor cortex ROI (PMC); and a single primary sensorimotor cortex, SM1 (23). Medial cortical structures, the anterior, medial, and posterior cingulate cortices (aCGc, mCGc, and pCGc, respectively) and precuneus were each individually treated. Last, posterior brain structures of the lateral surface were grouped into four components: an inferior posterior parietal cortex (iPPc) ROI that included the angular, supramarginal gyrus, and the inferior parietal lobe; a superior posterior parietal cortex (sPPc) ROI containing Brodmann's areas 5 and 7; the posterior third of the superior temporal gyrus (post-1/3 STS); and the primary visual cortex (V1). The remaining cortical regions were excluded from the current analysis. Because the AAL template does not separate the post-1/3 STS, this structure was manually defined for both NVs and BI subjects.

AAL cortices were regrouped for the frontal cortex into the following sets:

*i*) Orbitofrontal cortex (OFC): orbicular portions of the superior, medial and inferior frontal gyrus plus olfactory cortex, and gyrus rectus.
*ii*) Ventromedial prefrontal cortex (vmPFC): frontal superior and superior medial.
*iii*) Dorsolateral prefrontal cortex (dlPFC): lateral middle frontal gyrus and pars triangularis of the inferior frontal gyrus.
*iv*) Premotor cortices (PMCs): supplementary motor area, precentral cortex, and the opercular part of the inferior frontal gyrus.
*v*) SM1: primary motor cortex and primary sensory cortices.

AAL cortical ROIs of the parietal cortex were regrouping into the following:

*vi*) Inferior posterior parietal cortex (iPPc): includes parietal inferior in association to the angular and supramarginal gyrus.
*vii*) Superior posterior parietal cortex (sPPc): parietal superior.
*viii*) Deep midline cortical structures such as the anterior, medial, and posterior cingulate cortices (aCGc, mCGc, and pCGc, respectively) and precuneus were individually treated. The primary visual cortex (V1) included the calcarine and cuneus. Last, the posterior third of the superior temporal gyrus (post-1/3 STS) was manually defined in NV and BI patients.


1. Schiff ND (2010) Recovery of consciousness after brain injury: A mesocircuit hypothesis. *Trends Neurosci* 33(1):1–9.
2. Mawlawi O, et al. (2001) Imaging human mesolimbic dopamine transmission with positron emission tomography: I. Accuracy and precision of D(2) receptor parameter measurements in ventral striatum. *J Cereb Blood Flow Metab* 21(9): 1034–1057.
3. Haber SN, Lynd E, Klein C, Groenewegen HJ (1990) Topographic organization of the ventral striatal efferent projections in the rhesus monkey: An anterograde tracing study. *J Comp Neurol* 293(2):282–298.
4. Selemon LD, Goldman-Rakic PS (1985) Longitudinal topography and interdigitation of corticostriatal projections in the rhesus monkey. *J Neurosci* 5(3):776–794.
5. Künzle H (1975) Bilateral projections from precentral motor cortex to the putamen and other parts of the basal ganglia. An autoradiographic study in Macaca fascicularis. *Brain Res* 88(2):195–209.
6. Tzourio-Mazoyer N, et al. (2002) Automated anatomical labeling of activations in SPM using a macroscopic anatomical parcellation of the MNI MRI single-subject brain. *Neuroimage* 15(1):273–289.
7. Schwarz ST, et al. (2011) T1-weighted MRI shows stage-dependent substantia nigra signal loss in Parkinson's disease. *Mov Disord* 26(9):1633–1638.
8. Delforge J, Bottlaender M, Loc'h C, Dolle F, Syrota A (2001) Parametric images of the extrastriatal D2 receptor density obtained using a high-affinity ligand (FLB 457) and a double-saturation method. *J Cereb Blood Flow Metab* 21(12):1493–1503.
9. Farde L, et al. (1997) A PET-study of [11C]FLB 457 binding to extrastriatal D2-dopamine receptors in healthy subjects and antipsychotic drug-treated patients. *Psychopharmacology (Berl)* 133(4):396–404.
10. Gurevich EV, Joyce JN (1999) Distribution of dopamine D3 receptor expressing neurons in the human forebrain: Comparison with D2 receptor expressing neurons. *Neuropsychopharmacology* 20(1):60–80.
11. Hall H, et al. (1996) Autoradiographic localization of extrastriatal D2-dopamine receptors in the human brain using [125I]epidepride. *Synapse* 23(2):115–123.
12. Mukherjee J, et al. (2002) Brain imaging of 18F-fallypride in normal volunteers: Blood analysis, distribution, test-retest studies, and preliminary assessment of sensitivity to aging effects on dopamine D-2/D-3 receptors. *Synapse* 46(3): 170–188.

13. Rieck RW, Ansari MS, Whetsell WO, Jr., Deutch AY, Kessler RM (2004) Distribution of dopamine D2-like receptors in the human thalamus: Autoradiographic and PET studies. *Neuropsychopharmacology* 29(2):362–372.
14. Broft A, et al. (2012) Striatal dopamine in bulimia nervosa: A PET imaging study. *Int J Eat Disord* 45(5):648–656.
15. Wu Y, Carson RE (2002) Noise reduction in the simplified reference tissue model for neuroreceptor functional imaging. *J Cereb Blood Flow Metab* 22(12):1440–1452.
16. Rousset OG, Ma Y, Evans AC (1998) Correction for partial volume effects in PET: principle and validation. *J Nucl Med* 39(5):904–911.
17. Tzourio-Mazoyer N, et al. (2002) Automated anatomical labeling of activations in SPM using a macroscopic anatomical parcellation of the MNI MRI single-subject brain. *Neuroimage* 15(1):273–289.
18. Wallis JD (2007) Orbitofrontal cortex and its contribution to decision-making. *Annu Rev Neurosci* 30:31–56.
19. Young L, et al. (2010) Damage to ventromedial prefrontal cortex impairs judgment of harmful intent. *Neuron* 65(6):845–851.
20. Katsuki F, Constantinidis C (2012) Early involvement of prefrontal cortex in visual bottom-up attention. *Nat Neurosci* 15(8):1160–1166.
21. Rowe J, Toni I, Josephs O (2000) The prefrontal cortex: Response selection or maintenance within working memory? *Science* 288(5471):1656–1660.
22. Sakai K (2008) Task set and prefrontal cortex. *Annu Rev Neurosci* 31:219–245.
23. Honda M, et al. (1998) Dynamic cortical involvement in implicit and explicit motor sequence learning. A PET study. *Brain* 121(Pt 11):2159–2173.

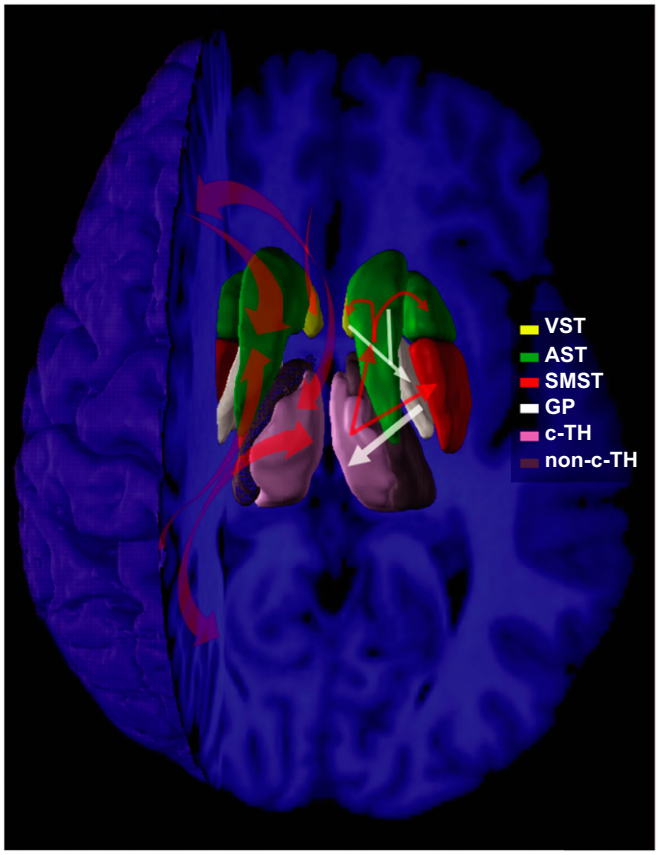


**Fig. S1.** Connectivity of segregated basal ganglia–thalamostriatal and thalamocortical mesocircuit.

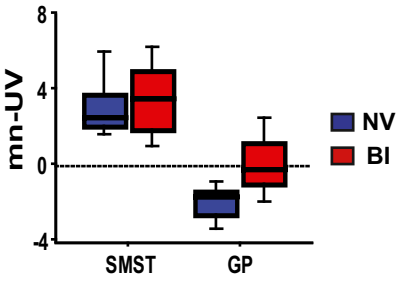


**Fig. S2.** Group data displaying results from partial volume effect (PVE) correction of the [$^{18}$F]FDG-PET. Box plot showing a significantly greater mn-UV within the GP for BI patients compared with the GP from NV. No difference between groups is present for the SMST (*$P < 0.001$).

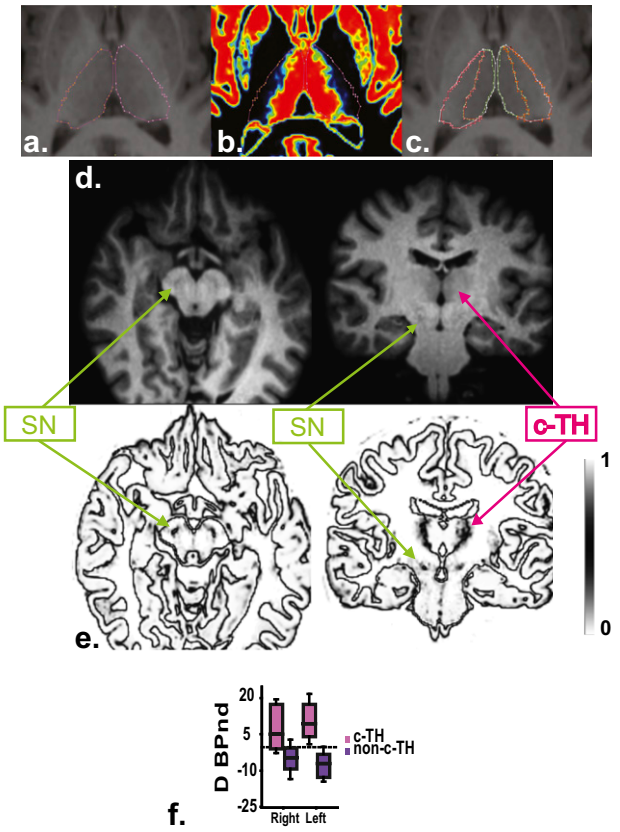


**Fig. S3.** (*A*) Manual delimitation of the entire TH in a NV. (*B*) Results of the GM automatic segmentation (red color indicates automatic assignment of gray matter). Note that half of the structure is missing from the automatic ROI. (*C*) Masking of the TH using the GM results to delimit the c-TH (green line) and non-c-TH (red line). (*D*) Axial and coronal views of a structural high definition T1 illustrating the similarities of the signal hypointensities of the SN and central aspect of the thalamus. (*E*) Results of the GM automatic segmentation displayed using a white-black-white scale to enhance middle range intensity signal verifying the similarity of SN and the central aspect of the thalamus signal characteristics. (*F*) Group data displaying results from [$^{11}$C]raclopride-PET in NV ($n = 8$). Box plot showing a significantly greater ΔBPnd within the c-TH compared with the non-c-TH of both hemispheres (ΔBPnd: delta change on binding potential nondisplaceable; $P < 0.01$). TH, thalamus; c-TH, central thalamus; non-c-TH, noncentral thalamus; SN, substantia nigra; GM, gray matter.

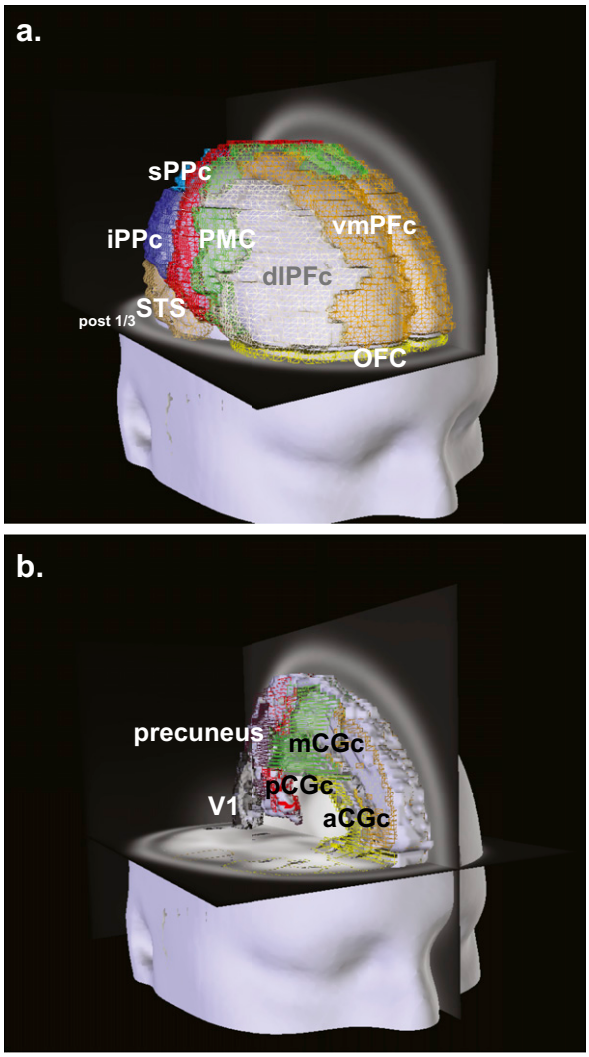


**Fig. S4.** Summary of cortical ROIs. (*A*) Anterior to posterior oblique view of right cortical ROIs on the lateral surface. (*B*) A similar display illustrating mesial deep cortical ROIs on the left surface.

**Table S1. Cortical glucose metabolism after severe BI**

| | Right hemisphere | | | | Left hemisphere | | | |
|---|---|---|---|---|---|---|---|---|
| ROI | NV | BI | *F* value | *P* value | NV | BI | *F* value | *P* value |
| OFc | 0.67 ± 0.09 | −0.25 ± 0.06 | 53.2 | <0.0001 | 0.70 ± 0.09 | −0.08 ± 0.06 | 38.7 | <0.0001 |
| vmPFc | 1.14 ± 0.08 | 0.04 ± 0.11 | 28.8 | <0.0001 | 1.18 ± 0.11 | −0.03 ± 0.10 | 42.9 | <0.0001 |
| dlPFc | 1.38 ± 0.12 | 0.03 ± 0.11 | 39.8 | <0.0001 | 1.31 ± 0.10 | 0.23 ± 0.10 | 35.9 | <0.0001 |
| PMC | 1.16 ± 0.07 | 0.28 ± 0.09 | 28.3 | <0.0001 | 0.99 ± 0.09 | 0.27 ± 0.09 | 18.3 | <0.0001 |
| SM1 | 0.83 ± 0.07 | 0.52 ± 0.09 | 3.5 | NS | 0.67 ± 0.07 | 0.53 ± 0.08 | 0.9 | NS |
| aCGc | −0.31 ± 0.11 | −0.13 ± 0.13 | 0.5 | NS | −0.31 ± 0.11 | −0.18 ± 0.11 | 0.2 | NS |
| mCGc | 0.81 ± 0.11 | −0.04 ± 0.16 | 8.5 | 0.0058 | −0.61 ± 0.28 | −0.14 ± 0.20 | 14.5 | 0.0005 |
| pCGc | −0.61 ± 0.28 | −0.61 ± 0.11 | 0.0 | NS | 0.81 ± 0.11 | −0.27 ± 0.16 | 15.2 | 0.0004 |
| Precuneus | 1.46 ± 0.15 | 0.41 ± 0.15 | 14.2 | 0.0005 | 1.46 ± 0.15 | 0.23 ± 0.12 | 46.8 | <0.0001 |
| sPPc | 0.98 ± 0.13 | −0.60 ± 0.15 | 33.5 | <0.0001 | 0.98 ± 0.10 | −0.21 ± 0.11 | 31.2 | <0.0001 |
| iPPc | 1.36 ± 0.12 | 0.33 ± 0.10 | 30.2 | <0.0001 | 0.98 ± 0.10 | 0.73 ± 0.08 | 2.8 | NS |
| post 1/3 STS | 1.39 ± 0.11 | 1.28 ± 0.23 | 0.8 | NS | 1.22 ± 0.13 | 1.72 ± 0.18 | 1.3 | NS |
| V1 | 1.80 ± 0.14 | 1.09 ± 0.19 | 4.0 | 0.048 | 2.36 ± 0.11 | 1.01 ± 0.20 | 14.2 | 0.0003 |

NS, not significant.

**Table S2. Patient demographic data**

| Patient | Age (y) | Sex | Etiology | CRS-R | Dx | Months postinjury | CF |
|---|---|---|---|---|---|---|---|
| BI-1 | 39 | M | TBI | 23 | EMCS | 233.5 | — |
| BI-2 | 23 | M | TBI | N/R | MCS | 72.0 | No |
| BI-3 | 55 | F | SAH | N/R | MCS | 18.6 | — |
| BI-4 | 22 | M | TBI | 6 | MCS | 41.9 | No |
| BI-5 | 39 | M | TBI | 11 | MCS | 253.5 | No |
| BI-6 | 40 | F | CVA | 9 | MCS | 21.5 | No |
| BI-7 | 57 | F | CVA | 11 | MCS | 49.4 | Yes |
| BI-3 | 56 | F | SAH | N/R | MCS | 32.9 | — |
| BI-8 | 58 | F | AE | 14 | MCS | 12.2 | No |
| BI-9 | 25 | F | TBI | 14 | MCS | 24.4 | Yes |
| BI-10 | 43 | M | TBI | 23 | EMCS | 63.9 | — |
| BI-11 | 18 | F | TBI | 14 | MCS | 5.8 | Yes |
| BI-12 | 54 | M | TBI | 16 | MCS | 257.0 | Yes |
| BI-13 | 27 | F | TBI | 15 | MCS | 56.9 | Yes |
| BI-8 | 59 | F | AE | 15 | MCS | 19.4 | Yes |
| BI-11 | 19 | F | TBI | 19 | MCS | 9.4 | Yes |
| BI-14 | 40 | M | AE | 6 | VS | 70.7 | No |
| BI-15 | 31 | M | TBI | 11 | MCS | 50.6 | Yes |
| BI-5 | 39 | M | TBI | 11 | MCS | 276.9 | No |
| BI-8 | 60 | F | AE | 22 | MCS | 31.5 | Yes |
| BI-16 | 39 | M | MS | 10 | MCS | 48.9 | No |
| BI-16 | 39 | M | MS | 18 | MCS | 49.9 | Yes |
| BI-17 | 37 | M | TBI | 4 | VS | 64.2 | No |
| BI-18 | 53 | M | TBI | 22 | MCS | 9.7 | Yes |
| BI-6 | 42 | F | CVA | 13 | LIS/MCS | 53.1 | — |
| BI-19 | 40 | M | TBI | 14 | MCS | 61.0 | Yes |
| BI-20 | 53 | M | AE | 5 | VS | 37.1 | No |
| BI-5 | 43 | M | TBI | 13 | MCS | 294.5 | Yes |
| BI-21 | 31 | M | TBI | 6 | MCS | 9.4 | No |
| BI-22 | 26 | M | TBI | 5 | MCS | 110.2 | No |
| BI-23 | 55 | M | TBI | 11 | MCS | 60.1 | No |
| BI-24 | 27 | F | AE | 9 | MCS | 69.0 | No |

AE, anoxic-ischemic encephalopathy; BI, severe brain injury case number; CVA, cerebrovascular accident; EMCS, emerging from MCS; F, female; LIS, lock-in syndrome; M, male; MCS, minimally conscious state; N/R, not recorded; SAH, subarachnoid hemorrhage; TBI, traumatic brain injury; VS, vegetative state.